CHIN. PHYS. LETT. Vol. 37, No. 7 (2020) 077501

Site Preference of Se and Te in $Bi_2Se_{3-x}Te_x$ Thin Films

Yizhe Sun(孙逸哲)[1], Moorthi Kanagaraj[1], Qinwu Gao(高钦武)[1], Yafei Zhao(赵亚飞)[1], Jiai Ning(宁纪爱)[1], Kunpeng Zhang(张昆鹏)[2], Xianyang Lu(陆显扬)[1,2], Liang He(何亮)[1,3*], and Yongbing Xu(徐永兵)[1,2,3*]

[1]*National Laboratory of Solid State Microstructures and Jiangsu Provincial Key Laboratory of Advanced Photonic and Electronic Materials, School of Electronic Science and Engineering, Nanjing University, Nanjing 210093, China*

[2]*York-Nanjing Joint Center (YNJC) for Spintronics and Nano-engineering, University of York, York YO105DD, United Kingdom*

[3]*Collaborative Innovation Center of Advanced Microstructures, Nanjing University, Nanjing 210093, China*

(Received 20 March 2020; accepted 10 May 2020; published online 21 June 2020)

The ternary topological insulators $Bi_2Se_{3-x}Te_x$ have attracted a great deal of attention due to their exotic physical and chemical properties. While most of the studies focus on the properties of these ternary TIs, limited research was performed to investigate the dynamic atomic stack of its crystal structure. We prepared high-quality $Bi_2Se_{3-x}Te_x$ thin films on GaAs(111)B substrates using molecular beam epitaxy, characterized with Raman spectroscopy, x-ray diffraction and photoelectron spectroscopy. It is found that when Se is replaced by Te, the preferred substituting sites are the middle layer at $0 < x < 1$, and this is also valid for Se substituting Te at $2 < x < 3$. In the middle region, the substituting atoms prefer to go to the first and the fifth layer.

PACS: 75.78.−n, 75.47.Lx, 75.30.Ds DOI: 10.1088/0256-307X/37/7/077501

Topological insulators (TIs) such as bismuth telluride and bismuth selenium have a "conventional" energy gap in the bulk materials, but the surface hold gapless Dirac-like states, which are protected against any time-invariant perturbations such as crystal imperfections and impurities.[1,2] Three-dimensional (3D) TIs have attracted great interests in the last few decades[3–6] and results were reported in diverse experimental fields,[7] such as the applications for electronic,[8] optoelectronic[9] and thermoelectric devices.[10] Recently, ternary TIs such as the $Bi_2Se_{3-x}Te_x$ compound has demonstrated higher mobility,[11,12] larger surface contribution and enhanced thermoelectric performance,[13,14] compared with binary TIs.[15,16] However, the preferred atomic sites of Te substitution in the place of Se have not been explored thoroughly.[17,18] Therefore, it is important to investigate their structural evolution during the growth of such ternary TIs, which may help to understand the ternary TI $Bi_2Se_{3-x}Te_x$ system more clearly.

In this work, $Bi_2Se_{3-x}Te_x$ films of six quintuple layers (QLs) were grown on high resistivity ($\approx 10\,\mathrm{M\Omega\cdot cm}$) GaAs(111)B substrates using molecular beam epitaxy (MBE).[19] The base pressure of the MBE chamber is below 2×10^{-10} Torr. The GaAs(111)B substrates were cleaned before being loaded into the chamber.[20] Then the substrates were annealed at 580 ℃ in the growth chamber until the streak patterns appeared as monitored by the real-time reflection high-energy electron diffraction (RHEED).[21] High-purity Bi(99.9999%), Se(99.9999%) and Te(99.9999%) were evaporated by conventional effusion cells. During the growth, Bi effusion cell was kept at 525 ℃, Se and Te effusion cells were kept at different temperatures with a Ⅵ/Ⅴ vapor rate ratio of 10, where Ⅵ stands for Se and Te, Ⅴ refers to Bi. For Bi_2Se_3, Se cell was kept at 135 ℃; for $Bi_2Se_{2.1}Te_{0.9}$, Se and Te cells were kept at 125 ℃ and 230 ℃, respectively; for $Bi_2Se_{1.4}Te_{1.6}$, 115 ℃ and 240 ℃ were used, respectively; for $Bi_2Se_{0.7}Te_{2.3}$, 105 ℃ and 250 ℃ were used, respectively; for Bi_2Te_3, Te cell was kept at 260 ℃. The GaAs(111)B substrates were set at 165 ℃ for all the samples.

Figure 1(a) shows the representative RHEED patterns of all $Bi_2Se_{3-x}Te_x$ films. Sharp streaky patterns were observed on all $Bi_2Se_{3-x}Te_x$ films, which indicate flat surface morphology. Figure 1(b) shows a typical AFM (NT-MDT, Integra Spectra Ⅱ, probe aperture size ∼ 100 nm) image of an as-grown Bi_2Se_3 film with a thickness of 6 QLs. Characteristically triangle-shaped terraces were observed with a size of ∼200 nm, reflecting the hexagonal crystal structure inside the (0001) plane.[22] RHEED intensity oscillations were observed from the first layer of the growth, as shown in Fig. 1(c). It demonstrates a layer-by-layer growth mode,[21,23] and the growth rate is found to be 127 s/QL. Figure 1(d) illustrates the evolution of the *d*-spacing of $Bi_2Se_{3-x}Te_x$ films during growth. The horizontal black dashed line indicates the *d*-spacing of the GaAs(111)B substrate, the vertical green dashed line stands for the beginning of the growth. In addition, the finishing time of the first QL is shown by blue dashed line. This suggests that after the growth of the first layer, the films have completely released the stress and reached their intrinsic lattices of $Bi_2Se_{3-x}Te_x$ thin films.[6] In our experimental case, the stoichiometries were determined by the *d*-spacing

Supported by the National Key Research and Development Program of China (Grant No. 2016YFA0300803), the National Natural Science Foundation of China (Grant Nos. 61474061, 61674079, and 61974061), and the Jiangsu ShuangChuang Program and the Natural Science Foundation of Jiangsu Province of China (Grant No. BK20140054).

*Corresponding author. Email: heliang@nju.edu.cn; ybxu@nju.edu.cn

© 2020 Chinese Physical Society and IOP Publishing Ltd

of the RHEED, which is inversely proportional to the in-plane lattice constant. Meanwhile, the in-plane lattice constants a were calculated from d-spacing, which is shown in Fig. 1(e). It increases with the increasing Te concentration, which agrees well with the result reported.[24]

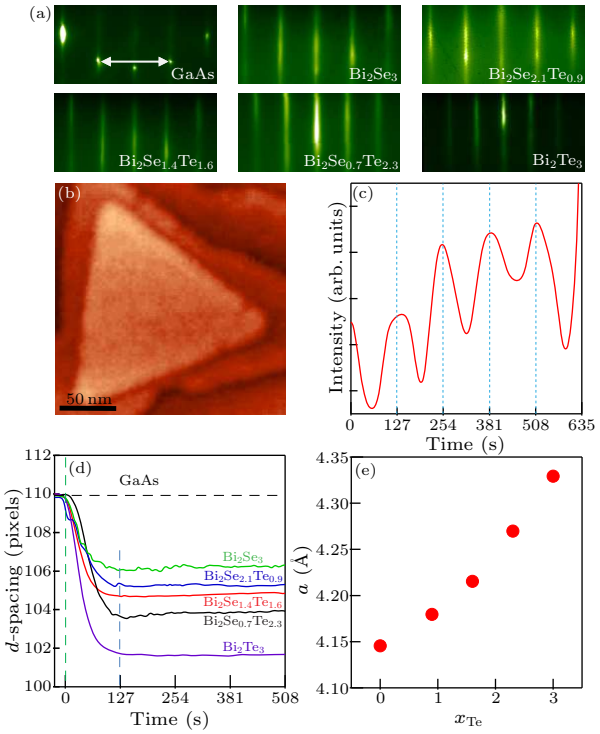

Fig. 1. (a) RHEED patterns of GaAs(111)B, Bi_2Se_3, $Bi_2Se_{2.1}Te_{0.9}$, $Bi_2Se_{1.4}Te_{1.6}$, $Bi_2Se_{0.7}Te_{2.3}$, Bi_2Te_3, respectively. The sharp diffraction streak pattern indicates the two-dimensional morphology and high quality of the film. The double-headed arrow between the two first-order stripes represents the d-spacing, which is inversely proportional to the in-plane lattice constant. (b) A typical AFM image of the as-grown Bi_2Se_3 film with thickness of 6 QLs. (c) RHEED oscillations demonstrate a layer-by-layer growth mode, indicating a growth rate of 127 s/QL. (d) The time evolution of the d-spacing of the films during growth. The horizontal black dashed line indicates the d-spacing of the GaAs(111)B substrate, the vertical green dashed line stands for the beginning of the growth, the blue dashed line shows the finishing time of the first QL. (e) The calculated lattice constant a of $Bi_2Se_{3-x}Te_x$ with various Te concentrations.

The phase purity and crystal structure of $Bi_2Se_{3-x}Te_x$ thin films have been identified by x-ray diffraction (Bruker D8 Discover single crystal diffractometer, $\lambda = 1.5406$ Å) and the spectra are shown in Fig. 2(a). Compared with the Joint Committee on Powder Diffraction Standards (JCPDS) data of Bi_2Se_3 and Bi_2Te_3, these films have been found to exhibit rhombohedral crystal geometry (space group $R\bar{3}m$ (D^5_{3d})) with no other detectable phases.[25] Overall, all the peaks shift to lower angles, as more Te substituted Se. Figure 2(b) shows a zoom-in view of the (006) peak. In Fig. 2(c), the lattice parameters c and the unit cell volume were calculated according to the position of the XRD peaks, the lattice parameter c (red) and unit cell volume (blue) increase monotonically, consistent with the previous reports.[26] Combined with the RHEED results, this demonstrates that the unit cells of $Bi_2Se_{3-x}Te_x$ thin films are expanded along the in-plane and out-of-plane directions while larger Te atoms replace Se atoms.[27] We have further characterized the elemental chemical states of $Bi_2Se_{3-x}Te_x$ films using monochromatic x-ray photoelectron spectroscopy (PHI 5000 Versa Probe system Al $k\alpha$) measurement at room temperature. The spectra are shown in Fig. S1 in the supplementary material. From the figure, Bi $4f$, Te $3d$ and Se $3d$ states can be observed,[28,29] suggesting the existence of $Bi_2Se_{3-x}Te_x$.

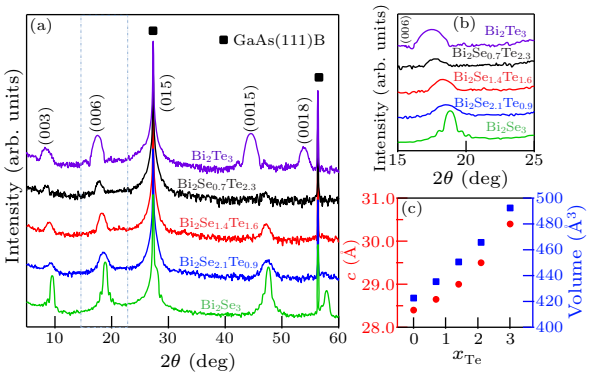

Fig. 2. (a) XRD patterns of $Bi_2Se_{3-x}Te_x$ ($x = 0, 0.9, 1.6, 2.3, 3$). (b) Expanded view showing a systematic shift of the (006) peak for $Bi_2Se_{3-x}Te_x$. (c) The calculated lattice parameters c (red) and unit cell volume V (blue) of $Bi_2Se_{3-x}Te_x$.

To investigate the vibrational properties and electron-phonon coupling in these layered compounds, Raman spectroscopy (Horiba Jobin-Yvon HR800) measurements were performed to understand the local structural changes for different Se:Te ratios.[30] It is known that the topological insulators were layered rhombohedral crystal, as shown in Fig. 3(a). There are five mono-atomic planes ($-A^1$–B–A^2–B–A^1-) which are covalently bonded to form five-atom thick layers, often referred to as one QL,[31,32] where A refers to either Se or Te, and B stands for Bi. On the other hand, these quintuple layers are weakly bonded to each other by the van der Waals force. Figure 3(b) shows the three Raman vibration modes of $Bi_2Se_{3-x}Te_x$ samples, A^1_{1g}, E^2_g and A^2_{1g}.[23] The A^1_{1g} mode is attributed to the synchronized movement of Bi and Se^1 (Te^1) along the out-of-plane direction, while A^2_{1g} and E^2_g correspond to the opposite movement of Bi and Se^1 (Te^1) along the in-plane and out-of-plane directions, respectively. For all of them, Se^2 (Te^2) is stationary. Thus, the Raman vibrations are sensitive to Te (Se) substituting at Se^1 (Te^1) position, but insensitive to Te (Se) substituting at Se^2 (Te^2) position.[33]

The Raman spectra of the $Bi_2Se_{3-x}Te_x$ samples with different Te concentrations in the wavenumber range 50–200 cm^{-1} measured at room temperature are shown in Fig. 3(c). Within the scanned frequency range, there are three characteristic peaks of 71 cm^{-1}, 132 cm^{-1} and 173 cm^{-1}, which correspond to A^1_{1g}, E^2_g

and A_{1g}^2 vibrational modes of Bi_2Se_3, respectively.[34] The peaks are shifted to the lower frequency with more Te incorporated. This can be attributed to the elongation of the chemical bonds between Bi and Te.[35] since Te has larger atomic size and weaker electronegativity compared with Se. It is interesting to note that Raman shift seems to demonstrate three regions (red, white and blue) for all the three peaks, as shown in Fig. 3(d).[36] This may give a hint of the site preference of Te substituting Se and vice versa.

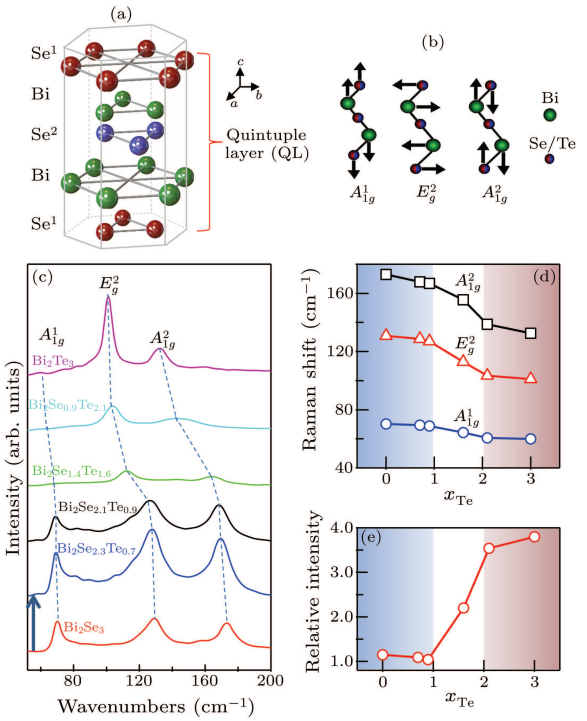

Fig. 3. (a) Crystal structure of rhombohedra Bi_2Se_3. (b) Schematic diagrams for the three Raman vibrational modes A_{1g}^1, E_g^2 and A_{1g}^2. (c) Raman spectra of $Bi_2Se_{3-x}Te_x$ thin films excited by a 514 nm laser. The graphs have been shifted vertically and equally for clarity, thus the peak position shifts to lower wavenumbers as Te concentration increases. (d) The dependence of Raman peak position on stoichiometric ratio. It can be observed that the Raman shifts are small in the blue ($x < 1$) and red ($x > 2$) regions, while it is much larger in the white ($1 < x < 2$) region for all the three peaks. (e) The relative intensity of E_g^2 to A_{1g}^2 with the Te concentration. It changes dramatically from ∼1 in the blue region to ∼3.6 in the red region.

As mentioned above, there are two atomic sites of Se in Bi_2Se_3, assigned as Se^1 and Se^2, as shown in Fig. 3(a).[37] The chemical bonding between Bi and Se^2 is of a pure covalent nature,[14] while it is a mixture of ionic and covalent bond between Bi and Se^1. Thus the binding energy of Bi–Se^1 is stronger than that of Bi–Se^2. Therefore, on the formation of $Bi_2Se_{3-x}Te_x$ compounds ($0 < x < 1$), Te atoms will preferentially replace Se at Se^2 sites first.[38] As discussed above, the three acoustic vibrations are insensitive to Te substituting in Se^2 sites.[39] Thus the peak positions remain relative constants, as shown by the blue region in Fig. 3(d). The slightly changes here are attributed to the larger bond length of Bi–Te^2 compared with Bi–Se^2. This argument is also suitable for the case that Se substitutes Te^2 site in $Bi_2Se_{3-x}Te_x$ compounds ($2 < x < 3$), corresponding to the red region shown in Fig. 3(d). When the Te concentration (x) lies between 1 and 2, a mixture of Se^1 and Te^1 exists in the films.[40] Thus the peak positions smoothly change from Bi_2Se_2Te to Bi_2SeTe_2, as shown by the white region in Fig. 3(d).[41] Previous works have found the similar results that there is a discontinuity in the revolution of Raman peaks from Bi_2Se_3 to Bi_2Te_3, of which the results provide useful insights in the realization of composition engineering and the understanding optical properties of Bi–Se–Te-based catalysts.[42] Here we have proposed a possible explanation to this slope change of the evolution of Raman peaks by the preferred substituting sites, which may further help to understand the precise structure of the ternary compound of $Bi_2Se_{3-x}Te_x$.

Furthermore, the relative intensity of E_g^2 and A_{1g}^2 with the increasing Te concentration has also been investigated, as shown in Fig. 3(e). Similarly, it demonstrates a step-like feature. When the Te concentration x is within 0–1, the relative intensity stays near 1. For Se substituting Te^2 in $Bi_2Se_{3-x}Te_x$ compounds ($2 < x < 3$), the E_g^2 to A_{1g}^2 ratio stays near 3.6. And it rapidly changes in the middle region, suggesting that Te (Se) are substituting Se^1(Te^1) here.[43]

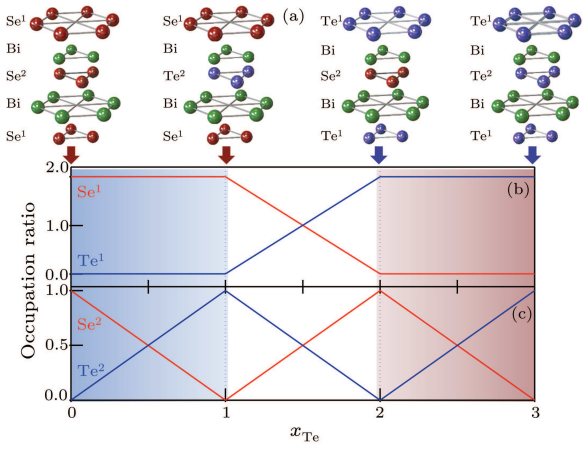

Fig. 4. (a) Schematic structures of Bi_2Se_3, Bi_2Se_2Te, Bi_2SeTe_2, Bi_2Te_3. (b) The occupational ratio of Se^1 (red line) and Te^1 (blue line) with the Te concentration. The occupational ratio of Se^1 stays at 2(0) and Te^1 stays at 0(2) when $0 < x < 1$ ($2 < x < 3$), as shown in the blue (red) region. In the middle region, Se^1 linearly decreases from 2 to 0 and Te^1 increases from 0 to 2. They are equal to 1 when $x = 1.5$. (c) The occupational ratio of Se^2 (red line) and Te^2 (blue line) with the Te concentration. The occupational ratio of Se^2 decreases from 1 to 0, while Te^2 increases from 0 to 1 when $0 < x < 1$. This reverses in $2 < x < 3$, as Se substitutes Te in Bi_2Te_3.

Figure 4(a) shows the schematic structures of Bi_2Se_3, Bi_2Se_2Te, Bi_2SeTe_2, Bi_2Te_3. The quintuple layer stackings of Bi_2Se_2Te and Bi_2SeTe_2 are Se^1–Bi–Te^2–Bi–Se^1 and Te^1–Bi–Se^2–Bi–Te^1, respectively.[44] The occupational ratios of Se^1, Te^1, Se^2 and Te^2 are shown in Figs. 4(b) and 4(c). When the Te concentration is within 0–1, the occupational ratio of Se^1 stays

at 2 while Te^1 remains at 0. The occupational ratio of Se^2 decreases from 1 to 0 as Te gradually substitutes Se at Se^2 sites, which is shown in the blue region. When the Te concentration is between 1 and 2, Te at Se^1 site increases from 0 to 2 while Te at Se^2 decreases from 1 to 0. When $x = 1.5$, the ratio of Se to Te is 1 for each layer. These results are also in compliance with Se substituting Te^2 in $Bi_2Se_{3-x}Te_x$ compounds ($2 < x < 3$), which is shown in the red region.

In summary, we have investigated the structural evolution and Raman spectra in high-quality $Bi_2Se_{3-x}Te_x$ thin films grown by MBE. While Se and Te continuously substitutes each other, a smooth change of lattice constant have been observed. Both analysis suggests that the $Bi_2Se_{3-x}Te_x$ or $Bi_2Te_{3-x}Se_x$ ternary compounds have the tendency to stay in the binary form of Bi_2Se_3 or Bi_2Te_3 when the substituting ratio x is lower than 1. Thus the preferred substituting sites are the middle layer of Se^2 or Te^2. As a result, the shifts of the Raman peaks demonstrate a step-like feature, and it changes dramatically in the middle concentration region ($1 < x < 2$). Our findings may help to understand the precise structure of the ternary compound of $Bi_2Se_{3-x}Te_x$, which may become a theoretical basis of promising device applications.

One can see the supplemental material for details of RHEED patterns, XRD peaks calculations, x-ray photoelectron spectroscopy characterization and the observed weak anti-localization effect by magnetoresistance measurements.

References

[1] Butler S Z, Hollen S M, Cao L, Cui Y, Gupta J A, Gutiérrez H R, Heinz T F, Hong S S, Huang J, Ismach A F, Johnston-Halperin E, Kuno M, Plashnitsa V V, Robinson R D, Ruoff R S, Salahuddin S, Shan J, Shi L, Spencer M G, Terrones M, Windl W and Goldberger J E 2013 *ACS Nano* **7** 2898

[2] Kou X F, He L, Xiu F X, Lang M R, Liao Z M, Wang Y, Fedorov A V, Yu X X, Tang J S, Huang G, Jiang X W, Zhu J F, Zou J and Wang K L 2011 *Appl. Phys. Lett.* **98** 242102

[3] Liu W, Xu Y, He L, van der Laan G , Zhang R and Wang K 2019 *Sci. Adv.* **5** aav2088

[4] Liu W, West D, He L, Xu Y, Liu J, Wang K, Wang Y, van der Laan G , Zhang R, Zhang S and Wang K L 2015 *ACS Nano* **9** 10237

[5] Liu W, He L, Xu Y, Murata K, Onbasli M C, Lang M, Maltby N J, Li S, Wang X, Ross C A, Bencok P, van der Laan G , Zhang R and Wang K L 2015 *Nano Lett.* **15** 764

[6] He L, Kou X and Wang K L 2013 *Phys. Status Solidi RRL* **7** 50

[7] Xiu F, Meyer N, Kou X, He L, Lang M, Wang Y, Yu X, Fedorov A V, Zou J and Wang K L 2012 *Sci. Rep.* **2** 669

[8] Zhang H, Liu C X, Qi X L, Dai X, Fang Z and Zhang S C 2009 *Nat. Phys.* **5** 438

[9] Kim Y, Chen X, Wang Z, Shi J, Miotkowski I, Chen Y P, Sharma P A, Lima Sharma A L, Hekmaty M A, Jiang Z and Smirnov D 2012 *Appl. Phys. Lett.* **100** 071907

[10] Qiao H, Yuan J, Xu Z, Chen C, Lin S, Wang Y, Song J, Liu Y, Khan Q, Hoh H Y, Pan C X, Li S and Bao Q 2015 *ACS Nano* **9** 1886

[11] Wang Z F, Su N and Liu F 2013 *Nano Lett.* **13** 2842

[12] Xiong J, Luo Y, Khoo Y, Jia S, Cava R J and Ong N P 2012 *Phys. Rev. B* **86** 045314

[13] Ren Z, Taskin A A, Sasaki S, Segawa K and Ando Y 2010 *Phys. Rev. B* **82** 241306

[14] Soni A, Yanyuan Z, Ligen Y, Aik M K K, Dresselhaus M S and Xiong Q 2012 *Nano Lett.* **12** 1203

[15] Teague M, Chu H, Xiu F X, He L, Wang K L and Yeh N C 2012 *Solid State Commun.* **152** 747

[16] Wang W, Li L, Zou W, He L, Song F, Zhang R, Wu X and Zhang F 2015 *Sci. Rep.* **5** 7931

[17] Lu X, Atkinson L J, Kuerbanjiang B, Liu B, Li G, Wang Y, Wang J, Ruan X, Wu J, Evans R F L, Lazarov V K, Chantrell R W and Xu Y 2019 *Appl. Phys. Lett.* **114** 192406

[18] Wang W, Zou W Q, He L, Peng J, Zhang R, Wu X S and Zhang F M 2015 *J. Phys. D* **48** 205305

[19] He L, Xiu F, Yu X, Teague M, Jiang W, Fan Y, Kou X, Lang M, Wang Y, Huang G, Yeh N C and Wang K L 2012 *Nano Lett.* **12** 1486

[20] Lu Y X, Claydon J S, Xu Y B, Thompson S M, Wilson K and van der Laan G 2004 *Phys. Rev. B* **70** 233304

[21] Liu Z, Brandt R, Hellwig O, Florez S, Thomson T, Terris B and Schmidt H 2011 *J. Magn. Magn. Mater.* **323** 1623

[22] Wang K, Liu Y, Wang W, Meyer N, Bao L H, He L, Lang M R, Chen Z G, Che X Y, Post K, Zou J, Basov D N, Wang K L and Xiu F 2013 *Appl. Phys. Lett.* **103** 031605

[23] Lang M, He L, Xiu F, Yu X, Tang J, Wang Y, Kou X, Jiang W, Fedorov A V and Wang K L 2012 *ACS Nano* **6** 295

[24] Liu R, Tan X, Ren G, Liu Y, Zhou Z, Liu C, Lin Y and Nan C 2017 *Crystals* **7** 257

[25] Zhang J, Peng Z, Soni A, Zhao Y, Xiong Y, Peng B, Wang J, Dresselhaus M S and Xiong Q 2011 *Nano Lett.* **11** 2407

[26] Amaladass E P, Devidas T R, Sharma S, Sundar C S, Mani A and Bharathi A 2016 *J. Phys.: Condens. Matter* **28** 075003

[27] Devidas T R, Abhirami S, Sharma S, Amaladas E P and Mani A 2018 *Europhys. Lett.* **121** 67001

[28] Xiao C, Qin X, Zhang J, An R, Xu J, Li K, Cao B, Yang J, Ye B and Xie Y 2012 *J. Am. Chem. Soc.* **134** 18460

[29] Zhao Y and Burda C 2009 *ACS Appl. Mater. & Interfaces* **1** 1259

[30] Yuan J, Zhao M, Yu W, Lu Y, Chen C, Xu M, Li S, Loh K and Qiaoliang B 2015 *Materials* **8** 5007

[31] Kou X F, Jiang W J, Lang M R, Xiu F X, He L, Wang Y, Wang Y, Yu X X, Fedorov A V, Zhang P and Wang K L 2012 *J. Appl. Phys.* **112** 063912

[32] Xiu F, He L, Wang Y, Cheng L, Chang L T, Lang M, Huang G, Kou X, Zhou Y, Jiang X, Chen Z, Zou J, Shailos A and Wang K L 2011 *Nat. Nanotechnol.* **6** 216

[33] Shahil K M F, Hossain M Z, Goyal V and Balandin A A 2012 *J. Appl. Phys.* **111** 054305

[34] Steinberg H, Laloë J B, Fatemi V, Moodera J S and Jarillo-Herrero P 2011 *Phys. Rev. B* **84** 233101

[35] Zhang G, Qin H, Teng J, Guo J, Guo Q, Dai X, Fang Z and Wu K 2009 *Appl. Phys. Lett.* **95** 053114

[36] Chis V, Sklyadneva I Y, Kokh K A, Volodin V A, Tereshchenko O E and Chulkov E V 2012 *Phys. Rev. B* **86** 174304

[37] Zhao S Y F, Beekman C, Sandilands L J, Bashucky J E J, Kwok D, Lee N, LaForge A D, Cheong S W and Burch K S 2011 *Appl. Phys. Lett.* **98** 141911

[38] Wiese J and Muldawer L 1960 *J. Phys. Chem. Solids* **15** 13

[39] Bao L, He L, Meyer N, Kou X, Zhang P, Chen Z G, Fedorov A V, Zou J, Riedemann T M, Lograsso T A, Wang K L, Tuttle G and Xiu F 2012 *Sci. Rep.* **2** 726

[40] Benjamin S L, de Groot C K, Gurnani C, Hawken S L, Hector A L, Huang R, Jura M, Levason W, Reid E, Reid G 2018 *J. Mater. Chem. C* **6** 7734

[41] Checkelsky J G, Hor Y S, Cava R J and Ong N P 2011 *Phys. Rev. Lett.* **106** 196801

[42] Wu P, Chen H, Yang C, Gan W, Muhammad Z and Song L 2016 *AIP Adv.* **6** 075303

[43] Richter W and Becker C R 1977 *Phys. Stat. Sol. (b)* **84** 619

[44] Cava R J, Ji H, Fuccillo M K, Gibson Q D and Hor Y S 2013 *J. Mater. Chem. C* **1** 3176

Supplemental materials for "Site preference of Se and Te in $Bi_2Se_{3-x}Te_x$ thin films"

Yizhe Sun(孙逸哲),[1] Moorthi Kanagaraj,[1] Qinwu Gao(高钦武),[1] Yafei Zhao(赵亚飞),[1] Jiai Ning(宁纪爱),[1] Kunpeng Zhang(张昆鹏),[2] Xianyang Lu(陆显扬),[1,2] Liang He(何亮),[1, 3, a)] and Yongbing Xu(徐永兵),[1, 2, 3, b)]

[1]*National Laboratory of Solid State Microstructures and Jiangsu Provincial Key Laboratory of Advanced Photonic and Electronic Materials, School of Electronic Science and Engineering, Nanjing University, Nanjing 210093, China*

[2]*York-Nanjing Joint Center (YNJC) for Spintronics and Nano-engineering, University of York, York YO105DD, United Kingdom*

[3]*Collaborative Innovation Center of Advanced Microstructures, Nanjing University, Nanjing 210093, China*

Corresponding authors. E-mail: heliang@nju.edu.cn; ybxu@nju.edu.cn

i) X-Ray Diffraction

X-Ray diffraction measurements were done to all $Bi_2Se_{3-x}Te_x$ thin films. These films have found to exhibit rhombohedral crystal structure with space group $R\bar{3}m\left(D_{3d}^5\right)$. Lattice parameter *c* for the rhombohedral crystal can be calculated from X-ray diffraction peaks using the equation below:[1]

$$\frac{1}{d_{hkl}^2} = \frac{4}{3}\left(\frac{h^2 + hk + k^2}{a^2}\right) + \frac{l^2}{c^2}$$

Here, *a* and *c* are lattice constants, *hkl* are lattice indices for the crystal planes, λ

is the x-ray wavelength (1.5404 Å for Cu k_α).

ii) X-ray Photoelectron Spectroscopy

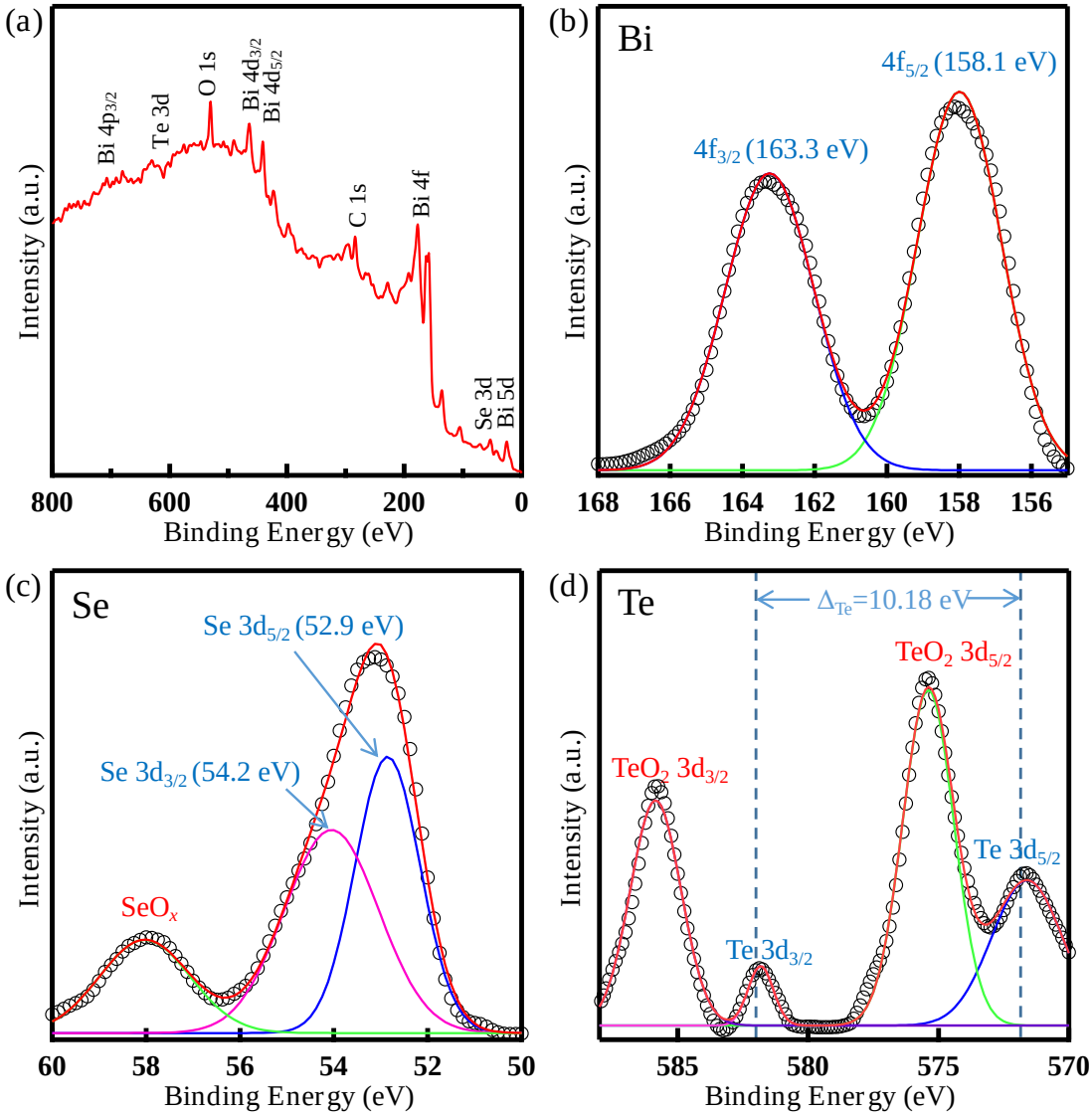

FIG. S1 XPS spectra of $Bi_2Se_{2.1}Te_{0.9}$ thin film: (a) survey spectra; (b) high-resolution spectra of Bi 4f, Se 3d (c) and Te 3d (d) photoemission lines.

Fig. S1 (a) shows the XPS spectrum of $Bi_2Se_{2.1}Te_{0.9}$ thin film, the carbon 1s peak was observed at the binding energy 284 eV, which is consistent with the standard peak position.[2] The high-resolution scan of the Bi 4f region shows peaks at about 158.1 eV

and 163.3eV in figure S1 (b), which correspond to the binding energies of Bi $4f_{5/2}$ and Bi $4f_{3/2}$, respectively.[3] In the Se 3d spectrum, two peaks can be observed by fitting of deconvolution peaks, one with a binding energy of 52.9 eV (corresponding of Se $3d_{5/2}$) and the other with 54.2 eV (corresponding of Se $3d_{3/2}$).[4] Along with the two peaks, there have been an additional SeO_x peaks present in around 58 eV[5,6], as shown in Figure S1 (c). Figure S1 (d) shows the XPS spectra of Te. It is found that due to air exposure after the growth, Te is strongly bind with oxygen, thus form TeO_x ($3d_{5/2}$ and $3d_{3/2}$) with higher binding energies than Te ($3d_{5/2}$ and $3d_{3/2}$) peaks. In addition, no peak of other elements is observed in the wide XPS survey spectrum.

iii) Magnetoresistance measurement

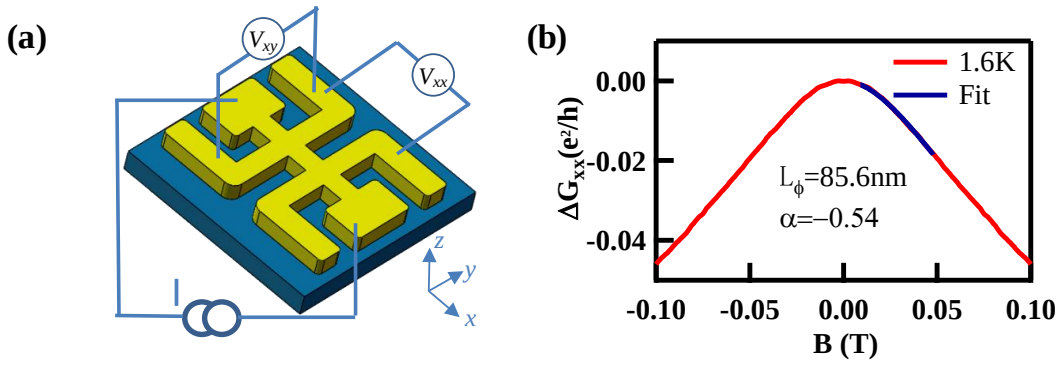

FIG S2 (a) Schematic diagram of Hall bar device for the samples, with the size of $L \times W = 1$ mm $\times$ 1 mm. A standard six-point measurement was carried out with constant AC current flow of 1 μA. (b) Trace of sheet magnetoconductance's change at 1.6 K, the blue lines are fits of 2D localization theory, where α is -0.54, and $l_\emptyset$ is 85.6 nm, confirming the 2D nature of WAL.

iv) Weak anti-localization (WAL) effect of $Bi_2Se_{3-x}Te_x$ thin films.

The quantum correction to the 2D magneto-conduction can be described by the Hikami-Larkin-Nagaoka (HLN) model below:[7]

$$\Delta G_{WAL}(B) = G(B) - G(0) = \frac{\alpha e^2}{2\pi^2 \hbar}\left[\Psi\left(\frac{1}{2} + \frac{B_\emptyset}{B}\right) - \ln\left(\frac{B_\emptyset}{B}\right)\right]$$

where Ψ is the digamma function, the prefactor α can be a WAL coefficient and should be equal to -0.5 for the topological surface states, *e* is the electric charge, ħ is the reduced Planck's constant, $B_\emptyset = \hbar / 4el_\emptyset^2$ is a magnetic field characterized by coherence length $l_\emptyset (l_\emptyset = \sqrt{D\tau_\emptyset}$, D is diffusion constant, $\tau_\emptyset$ is dephasing time).[8]

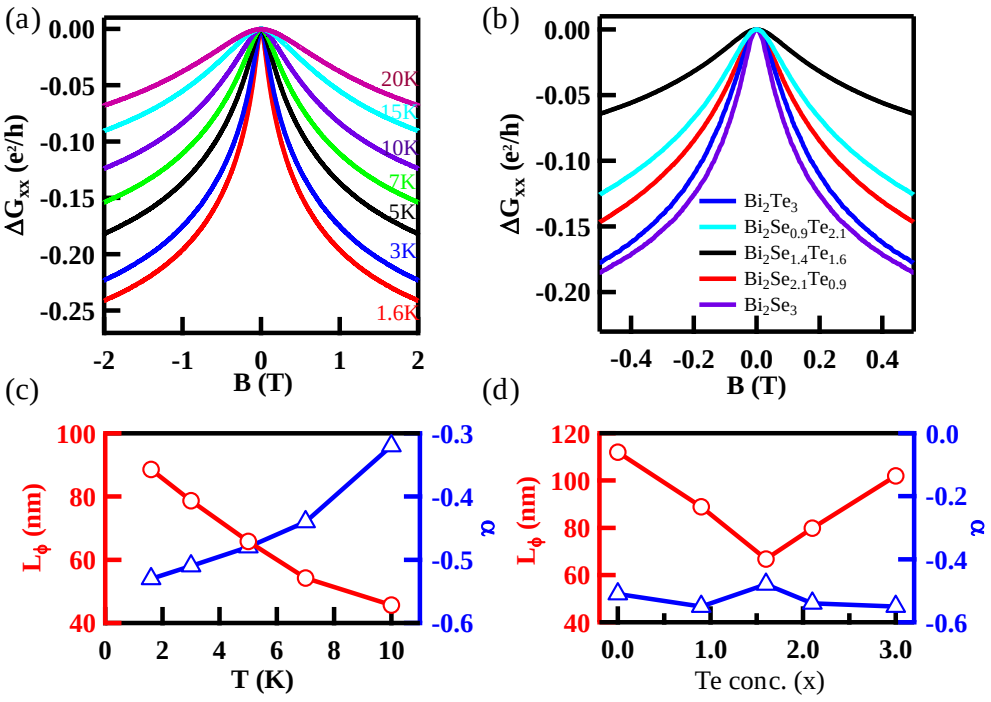

FIG S3 (a) The change of film magnetic conductance (ΔG_{xx}) in perpendicular magnetic fields at temperatures ranging from 1.6K to 20K of $Bi_2Se_{2.1}Te_{0.9}$, it shows the WAL features (sharp cusps at around zero magnetic field) persistent until 20K, (b) The change of film magnetic conductance (ΔG_{xx}) with the different Se concentration at 1.6K. (c) Figure shows the temperature dependence of L_φ (red circle) and α (blue triangle) of $Bi_2Se_{2.1}Te_{0.9}$ film. (d) The Te concentration dependence of L_φ (red circle) and α (blue triangle) of $Bi_2Se_{3-x}Te_x$ thin films at 1.6K.

Fig. S3 (b) demonstrates the ΔG_{xx} vs B of $Bi_2Se_{3-x}Te_x$ thin films at 1.6 K, it can be observed that each sample exhibits the characteristics of WAL effect. The results of HLN fitting were shown in Fig. S3(d)[9]. The value of coherence length $l_\emptyset$ (red circle)

decreases with the increase doping concentration. This may probably due to that the doping introduce the impurity into the bulk structure, which influence the topological characteristics. However, the value of α (blue triangle) almost keeps the same, this suggests that it maintain the 2D nature both in the binary and ternary topological insulators.

Reference

1. L. Rui, T. Xing, G. Ren, Y. Liu, Z. Zhou, L. Chan, Y. Lin and C. Nan, Crystals **7**, 257 (2017).
2. A. Gupta, R. K. Chowdhury, S. Ray and S. Srivastava, Nanotechnology **30** , 435204 (2019).
3. C. Xiao, X. Qin, J. Zhang, R. An, J. Xu, K. Li, B. Cao, J. Yang, B. Ye and Y. Xie, J. Am. Chem. Soc. **134**, 18460 (2012).
4. X. Yang, W. Xiong and Z. Zhang, J. Cryst. Growth **276**, 566 (2005).
5. Joseph A Hagmann et al, New J. Phys. **19** 085002 (2017).
6. Avery J. Green et al., Journal of Vacuum Science & Technology A 34, 061403 (2016).
7. S. Hikami, A. I. Larkin and Y. Nagaoka, Prog. Theor. Phys. **63**, 707 (1980).
8. L. He, X. Kou, M. Lang, E. S. Choi, Y. Jiang, T. Nie, W. Jiang, Y. Fan, Y. Wang, F. Xiu and K. L. Wang, Sci. Rep. **3**, 3406 (2013).
9. M. Lang, L. He, X. Kou, P. Upadhyaya, Y. Fan, H. Chu, Y. Jiang, J. H. Bardarson, W. Jiang, E. S. Choi, Y. Wang, N.-C. Yeh, J. Moore and K. L. Wang, Nano Lett. **13**, 48 (2013).